ISSN 1392-1320 MATERIALS SCIENCE (MEDŽIAGOTYRA). Vol. XX, No. X. 2027

Enhancing Mechanical and Corrosion Properties of a $Cr_9Fe_{46}Ni_{15}Mn_{30}$ Medium-Entropy Alloy through Synergistic Al/Ti Microalloying and Aging

Yuanji SHI [1, 2 *], Jianjun LIN [3], Zicheng LIN [3], Shebing LI [3], Min LIU [4], Jiawei WU [1], Zimo LI [1], Yan HU [1]

[1] *Industrial Perception and Intelligent Manufacturing Equipment Engineering Research Center, Nanjing University of Industry Technology, Nanjing, P.R. China*
[2] *Xinjiang Vocational University, Urumqi, P.R. China*
[3] *Longquan Zhongtai Auto Air Conditioner Co., Ltd., Lishui, P.R. China*
[4] *Faculty of Materials Technology, Shanghai Institute of Technology, Shanghai, PR China*

http://doi.org/10.5755/j02.ms.43602

Received 14 November 2025; accepted 12 January 2026

This study systematically investigates the synergistic effects of Al/Ti microalloying and subsequent aging treatment on the microstructure and properties of the $Cr_9Fe_{46}Ni_{15}Mn_{30}$ high-entropy alloy. The results demonstrate that Al and Ti additions induce pronounced grain refinement, reducing the average grain size from 5.2 μm to 1.52 μm, promote the formation of nanoscale Al/Ti-rich precipitates together with ~0.7 % body-centered cubic (BCC) phase, and decrease the recrystallization fraction to 92.1 %. Subsequent aging at 600 °C further improves microstructural homogeneity, increases the recrystallization fraction to 99.2 %, and reduces the kernel average misorientation (KAM) to 0.07°. Mechanical testing reveals that microalloying enhances the tensile strength to 708 MPa and significantly lowers the hydrogen embrittlement sensitivity index (δH) to 2.6 %. After aging, a pronounced hydrogen-induced plasticity effect is observed, with δH decreasing to −16.8 % and the elongation after hydrogen charging increasing to 29.2 %. In addition, the aged Al/Ti-microalloyed alloy exhibits superior corrosion resistance, characterized by the most positive corrosion potential (−0.279 V), the lowest corrosion current density (6.39×10^{-7} A·cm^{-2}), and the largest capacitive arc radius in electrochemical impedance spectroscopy. These improvements are attributed to the formation of a stable Cr_2O_3 passive film and a reduced defect density.

Keywords: CrFeNiMn system, medium-entropy alloy, hydrogen embrittlement sensitivity, corrosion resistance.

1. INTRODUCTION

With the growing demand for environmentally sustainable energy, the application of fuel-cell-powered transportation systems, such as automobiles and ships, has significantly accelerated the consumption of hydrogen and other green energy sources. However, during hydrogen storage, transportation, and refueling, metallic components exposed to hydrogen-rich environments for extended periods are susceptible to hydrogen ingress into the material matrix. This process can induce hydrogen embrittlement [1, 2] (HE), leading to premature fracture before reaching the theoretical tensile strength. Such service conditions impose stringent requirements on metallic materials, which must not only exhibit excellent resistance to hydrogen embrittlement but also retain reliable mechanical performance at cryogenic temperatures. In contrast, conventional metallic materials – including high-strength steels, high-manganese steels, aluminum alloys, and nickel-based alloys – are generally prone to hydrogen embrittlement, thereby posing significant risks to the structural integrity of engineering applications. Benefiting from their unique compositional design concepts, medium- and high-entropy alloys (M/HEAs) demonstrate outstanding mechanical properties across a wide temperature range, from cryogenic to elevated temperatures. These distinctive advantages position M/HEAs as highly promising candidates for overcoming hydrogen embrittlement, and consequently, they have emerged as a rapidly growing research focus [3, 4].

Yang et al. [5] demonstrated that lattice distortion in high-entropy alloys (HEAs) can markedly enhance both strength and toughness, while also exerting a significant influence on microstructure and deformation mechanisms. Kumar et al. [6] pointed out that when CoCrCuFeNiSix high-entropy alloys are prepared through two processes of discharge plasma sintering and vacuum arc smelting, the effect of Si content on the evolution and mechanical properties of the alloy phase. It is found that the addition of Si will promote the formation of specific phases and improve the hardness and wear resistance of the alloy. For instance, He et al. [7] developed a $(CrCoFeNi)_{94}Ti_2Al_4$ HEA by adding Ti and Al into the CrCoFeNi matrix. Through precise control of the subsequent processing route, a homogeneous distribution of γ precipitates was achieved, enabling the alloy to attain a tensile strength exceeding 1 GPa while maintaining an elongation of 40 %. Similarly, Qin et al. [8] designed a dual-FCC structured HEA, $Co_9Cr_7Cu_{36}Mn_{25}Ni_{23}$ (at.%), reinforced by nanoscale precipitates. Computational results indicated that the shear modulus mismatch and lattice distortion between the

* Corresponding author: Y.J. Shi
E-mail: *shiyj@niit.edu.cn*

nanoparticles and the matrix contributed to a strength increment of 419 MPa. Moreover, the combined effects of grain boundary strengthening and solid solution strengthening yielded a tensile yield strength of 401 MPa and an elongation of 36 %. Takeuchi et al.[9] pointed out that the Si content improves the hardness and wear resistance of the alloy by influencing phase evolution (such as promoting the formation of the σ phase and Ni_3Si phase) under the two processes of discharge plasma sintering and vacuum arc melting, and the performance of discharge plasma sintering samples is better. Likewise, Bohaiwa et al. [10] suggested that the addition of appropriate amounts of Al and Ti into FeNiCoCr-based HEAs enhances the chemical driving force for L12 precipitation, promoting the instability of the supersaturated FCC matrix toward Ni_3(Al,Ti)-type L12 and σ phases, thereby improving alloy strength, with a compressive strain as high as 47 %.

Meanwhile, Luo et al. [11] reported that CoNiV medium-entropy alloys exhibited negligible hydrogen embrittlement under a strain rate of 10-4 s^{-1} in a hydrogen environment. Li et al.[12] further confirmed that in FeCrCoNi high-entropy alloys, increasing the Fe content from 2.5 % to 25 % reduced hydrogen-induced plasticity loss from 70 % to 6 %, while the fracture mode shifted from intergranular brittle fracture to typical transgranular ductile fracture. Related studies have highlighted that CrFeMnNi-based medium- and high-entropy alloys possess excellent resistance to hydrogen embrittlement. For instance, Kwon et al. [13] demonstrated that CoCrFeMnNi HEAs fabricated via cryogenic rolling not only achieved an ultrahigh tensile strength of approximately 1.7 GPa, but also exhibited superior hydrogen embrittlement resistance, attributed to the combined effects of sluggish hydrogen diffusion, high hydrogen threshold at twin boundaries, and the absence of martensitic transformation. Li et al. [14] further indicated that the yield strength of CoCrFeMnNi alloys decreases initially and then increases with prolonged hydrogen charging time, which is associated with the competing effects of hydrogen-induced softening and hydrogen-enhanced twinning; moreover, hydrogen-assisted cracking was observed to initiate at grain boundaries and slip bands. Notably, Chen et al. [15] demonstrated that the introduction of C and Nb into equiatomic FeNiCoCr HEAs promoted the precipitation of nanoscale NbC particles. When the hydrogen concentration reached 4.3×10^{-6}, the plasticity loss was only 4.4 %, significantly lower than the 15.3 % observed in the unmodified alloy. In addition, Cheng et al. [16] developed a $(FeCoNi)_{86}Al_7Ti_7$ HEA with a dual-phase microstructure consisting of grain boundary L21 phases and intragranular L12 precipitates. The addition of Al and Ti endowed the alloy with a tensile strength exceeding 1300 MPa, while after 24 h of electrochemical hydrogen charging, the alloy maintained stable strength with only a 16 % reduction in elongation.

In this context, medium- and high-entropy alloys (M/HEAs) can be tailored by adjusting elemental compositions, particularly through microalloying with elements such as Al, Ti, and Nb. Such modifications not only enhance lattice distortion effects but also optimize the interactions between hydrogen and microstructural features, including precipitates and grain boundaries, thereby improving hydrogen embrittlement resistance. However, systematic investigations on the effects of Al/Ti microalloying on the microstructure, mechanical properties, and corrosion behavior of CrFeNiMn-based medium-entropy alloys remain limited. To address this gap, the present study focuses on the $Cr_9Fe_{46}Ni_{15}Mn_{30}(-Al_xTi_y)$ system (x = 0, 4; y = 0, 2). Through comprehensive microstructural characterization, hydrogen-charging tensile testing, and polarization measurements, the influence of Al/Ti elements on phase stability, hydrogen embrittlement susceptibility, and corrosion resistance is elucidated, providing a scientific basis for the composition and heat treatment process design of high-performance hydrogen-resistant alloys.

2. EXPERIMENTAL

2.1. Materials preparation

The experimental raw materials were Co, Cr, Fe, Ni, Mn, Al, and Ti metallic particles with a purity of ≥ 99.9 % and particle sizes of 1 – 5 mm, the raw materials were weighed using an electronic balance with a precision of ± 0.005 g (each element was weighed three times). The weighed materials were subsequently ultrasonically cleaned in ethanol, dried, and sealed for preservation. The alloys were prepared by vacuum arc melting. The raw materials were melted under an argon atmosphere, and after complete melting and solidification, the ingots were remelted five times with flipping to ensure chemical homogeneity. Subsequently, the alloys were homogenized at 1100 °C for 6 h in a GSL-1600X vacuum tube furnace, followed by air cooling to room temperature. The designed alloy compositions were $Cr_9Fe_{46}Ni_{15}Mn_{30}$(-AlxTiy) (x = 0, 4; y = 0, 2), which were designated as Mn_{30} and Mn_{30}-AlTi, respectively. All alloys were subjected to annealing at 900 °C, then it is used to cool slowly with the furnace, so as to eliminate internal stress and stabilize the organization. After cooling to a specific temperature in the furnace, take it out and cool it in the air. For 1 h prior to performance testing, and the corresponding samples were denoted as Mn30-T and Mn30-AlTi-T. Furthermore, the Mn30-AlTi-T sample was subjected to an aging treatment at 600 °C for 4 h and subsequently designated as Mn_{30}-AlTi-TA.

2.2. Microstructure and phase analysis

The specimens were sequentially ground with 80# to 2000# SiC abrasive papers, followed by mechanical polishing to a mirror finish using 1.5 μm diamond paste on a nylon polishing cloth. The polished samples were etched in aqua regia solution for 10 s, rinsed with deionized water and absolute ethanol, and subsequently examined using an LWD200-4XC optical microscope to observe the microstructures. Further microstructural characterization was conducted with a Zeiss Crossbeam XB 1540 scanning electron microscope (SEM), combined with energy-dispersive X-ray spectroscopy (EDS) to analyze and map the elemental distribution on the specimen surfaces.

After fine grinding, the specimens were electrolytically polished using a solution composed of 90 vol.% glacial acetic acid and 10 vol.% perchloric acid at an applied voltage of 27 V. The polishing duration was carefully

controlled through real-time observation of the surface using an optical microscope until an optimal surface finish was achieved. Subsequently, electron backscatter diffraction (EBSD) analyses were performed using a scanning electron microscope (SEM) equipped with an EDAX–TSL EBSD system. The observation surface corresponded to the two-dimensional plane defined by the rolling direction (RD) and the normal direction (ND). The EBSD measurements yielded crystallographic orientation distributions (inverse pole figures, IPFs), phase maps, spatial distributions of grain orientation spread (GOS) and kernel average misorientation (KAM), as well as the average grain size..

Phase analysis was conducted using a D/Max 2500 V X-ray diffractometer (Cu Kα radiation, λ = 0.1541 nm) operating at 20 mA and 30 kV. The specimens, with dimensions of 8.0 mm × 6.0 mm × 4.5 mm, were ground with 2000# sandpaper, ultrasonically cleaned in ethanol, and dried prior to testing. XRD measurements were performed over a 2θ range of 20° – 100° with a step size of 0.02° and a scanning rate of 5°/min. The diffraction patterns were analyzed using Jade 6.5 software.

2.3. Performance

After being ground with 2000# SiC abrasive paper, ultrasonically cleaned in ethanol for 10 min, and dried, the specimens were measured to calculate the hydrogen charging current. Electrochemical hydrogen charging was carried out in an electrolyte consisting of 0.5 mol/L H_2SO_4 + 1 g/L CH_4N_2S (with concentrated H_2SO_4 of 98 % purity). The CH_4N_2S acted as a hydrogen recombination poison, suppressing the formation of H_2 molecules and thereby facilitating hydrogen ingress into the material. The specimen served as the Working Electrode, while a platinum electrode was used as the Counter Electrode. Hydrogen charging was performed at a current density of 100 mA/cm² for 24 h. The schematic diagram of the hydrogen charging setup is shown in Fig. 1.

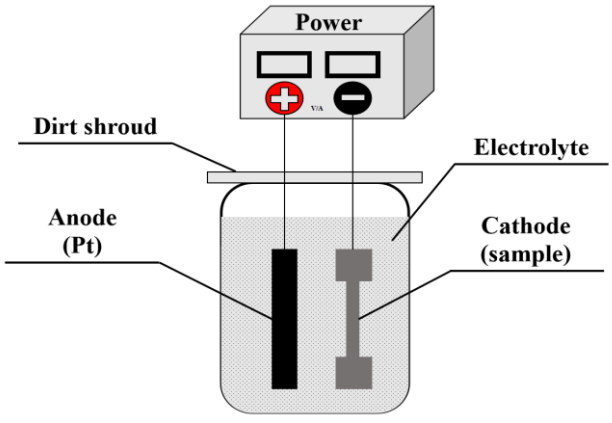

Fig. 1. Schematic diagram of electrochemical hydrogen charging

Slow strain rate tensile (SSRT) tests were conducted using an MST Criterion Model 44 universal testing machine to evaluate the mechanical properties and hydrogen embrittlement resistance of the alloys. The testing conditions followed the national standard GB/T 228.1-2010 for metallic tensile specimens. The specimens, prepared by wire electrical discharge machining (dimensions shown in Fig. 2), were ground with 240# to 2000# SiC abrasive papers, ultrasonically cleaned in ethanol, and then subjected to tensile testing at room temperature with a strain rate of 1×10^{-3} s^{-1}. Fracture morphologies were examined using a Zeiss Crossbeam XB 1540 scanning electron microscope. The hydrogen embrittlement susceptibility of the alloys was evaluated by comparing the elongation of hydrogen-charged and uncharged specimens under tensile loading, expressed in terms of plasticity loss rate (δH):

$$\delta_H = \frac{\Phi_{un} - \Phi_H}{\Phi_{un}} \times 100\%, \quad (1)$$

where δH is the hydrogen embrittlement sensitivity index; Φ_{un} is the elongation of the uncharged specimen; Φ_H is the the elongation of the hydrogen-charged specimen.

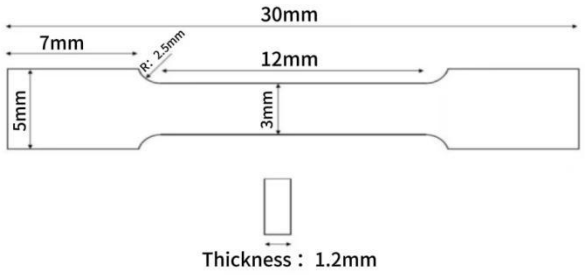

Fig. 2. Dimension of the tensile specimens

Further electrochemical measurements of the corrosion resistance of the alloys were carried out using a CHI660D electrochemical workstation. The tests were conducted in accordance with GB/T 40299-2021 “Corrosion of metals and alloys – Guidelines for electrochemical measurement methods of corrosion tests.” A three-electrode system was employed, with the specimen (12 mm × 12 mm × 5 mm) as the working electrode, a platinum sheet as the counter electrode, and a saturated calomel electrode (SCE) as the reference electrode. The electrolyte was a 3.5 wt.% NaCl solution at room temperature. Electrochemical impedance spectroscopy (EIS) measurements were conducted after stabilization of the open-circuit potential (OCP), with a sampling interval of 1 s. The electrochemical characterization comprised: 1) EIS measurements performed over a frequency range of 10^5 to 10^{-2} Hz, with the impedance data analyzed using ZView software; and 2) potentiodynamic polarization (Tafel) measurements carried out within a potential range of −0.5 to 1.0 V at a scan rate of 0.5 mV s^{-1}. Prior to the polarization tests, potentiostatic polarization was applied for 4 h to promote the formation of a stable passive film. The corrosion current density was subsequently determined by fitting the polarization curves.

3. RESULTS

3.1. Phase analysis

Fig. 3 presents the X-ray diffraction (XRD) patterns of the $Cr_9Fe_{46}Ni_{15}Mn_{30}$ medium-entropy alloy system, where Fig. 3 a corresponds to the rolled state and Fig. 3 b to the annealed state. According to previous studies [10, 17], the annealing condition for CrFeNiMn-based alloys was set at 900 °C for 1 h to ensure effective recrystallization. The XRD results reveal that, in the rolled state, all alloy compositions (Mn_{30} and Mn_{30}-AlTi) exhibit a single FCC

crystal structure without detectable diffraction peaks corresponding to intermetallic compounds or secondary phases. compromise the phase stability. Consequently, this indicates that, even under Al/Ti microalloying, the high-entropy effect effectively suppresses the formation of complex intermetallic phases. After annealing at 900 °C, all three alloys retained a stable single-phase FCC structure with no significant shifts in peak positions, demonstrating that the addition of Al/Ti did not, the CrFeNiMn-based medium-entropy alloy system exhibits excellent thermal stability. It is worth noting that previous research has reported that Al and Ti can promote B2, $L1_2$, or other ordered phases once the critical precipitation concentration is reached [10, 18]. However, no characteristic peaks of such ordered phases were observed in the diffraction patterns before or after heat treatment, which can be attributed to the ordered phases being either too finely dispersed or inhomogeneously distributed.

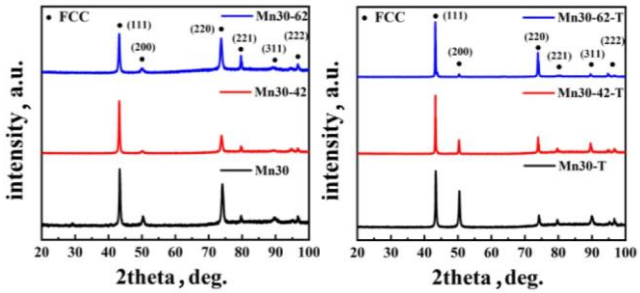

a b

Fig. 3. XRD pattern of the a – Mn30, Mn30-42 alloys; b – Mn30-T, Mn30-AlTi-T alloys

3.2. Microstructure analysis

Fig. 4 illustrates the microstructural evolution of Mn30-T and Mn30-AlTi-T specimens.

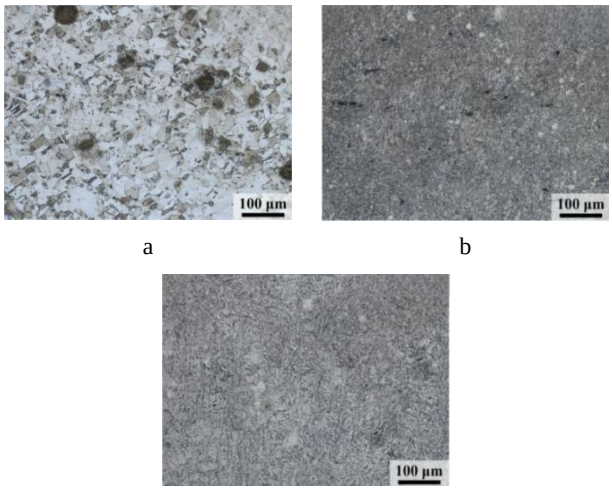

a b c

Fig. 4. OM microstructures of the a – Mn30-T; b – Mn30-AlTi-T; c – Mn30-AlTi-TA

Microstructural analysis reveals that the base alloy Mn30-T exhibits a typical fully recrystallized structure (Fig. 4 a), characterized by uniformly distributed equiaxed grains with a relatively large average grain size. The presence of well-defined grain boundaries indicates that the recrystallization process has been fully accomplished. In contrast, the Mn30-AlTi-T alloy displays a pronounced grain refinement compared with Mn30-T (Fig. 4 b). To elucidate the influence of alloying elements and heat treatment on the microstructural evolution of the $Cr_9Fe_{46}Ni_{15}Mn_{30}$ medium-entropy alloy, SEM coupled with EDS was employed to systematically characterize the grain boundary features, precipitate distribution, and elemental segregation behavior of Mn30-T, Mn30-AlTi-T, and Mn30-AlTi-TA specimens.

Fig. 5 presents the backscattered electron (BSE) microstructures and corresponding EDS elemental maps of the three specimens. As shown in Fig. 5 a, the base alloy Mn30-T exhibits a typical single-phase FCC structure composed of coarse equiaxed grains with an average size of approximately 10 μm. EDS area scans confirm that the constituent elements (Cr, Fe, Ni, Mn) are uniformly distributed throughout the matrix (Fig. 5 $a_1 – a_4$).In the Mn30-AlTi-T specimen (Fig. 5 b), numerous nanoscale precipitates are observed, with sizes ranging from 50 to 500 nm. EDS analysis identifies these precipitates as Al/Ti-enriched phases (Fig. 5 b_5, b_6), while the matrix elements (Cr, Fe, Ni, Mn) remain homogeneously distributed (Fig. 5 $b_1 – b_4$).

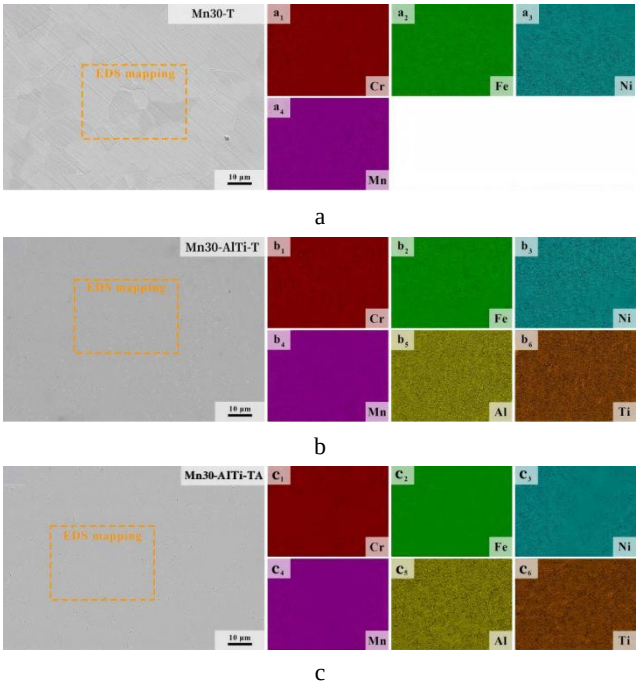

a b c

Fig. 5. SEM images and the corresponding EDS mappings of the a – Mn30-T; b – Mn30-AlTi-T; c – Mn30-AlTi-TA

Notably, some grains exhibit micron-sized voids due to precipitate detachment, and no dispersed precipitates are detected within the matrix, indicating that Al/Ti primarily form discrete enriched phases with clear precipitate–matrix interfaces and no significant elemental diffusion zones. These observations suggest that Al/Ti microalloying effectively promotes the formation of nanoscale secondary phases, and that the precipitate distribution is closely related to the alloy composition and heat treatment conditions. Fig. 5 c shows the microstructure and elemental distribution

of the Mn30-AlTi-TA alloy. EDS analysis indicates the presence of nanoscale precipitates (50 – 500 nm) uniformly distributed within the matrix, with sizes comparable to those in the solely annealed sample. Following aging treatment, the precipitates become more pronounced, with EDS confirming them as Al/Ti-enriched phases (Fig. 5 c_5, c_6), while the main matrix elements (Cr, Fe, Ni, Mn) remain homogeneously distributed (Fig. 5 $c_1 – c_4$). Therefore, aging alters the distribution characteristics of the precipitates, with grain boundaries acting as preferential nucleation sites for secondary phase formation, and the elemental partitioning behavior being jointly controlled by diffusion kinetics and interfacial energy [19].

Fig. 6 presents the inverse pole figure (IPF) maps and grain size statistics of Mn30-T, Mn30-AlTi-T, and Mn30-AlTi-TA specimens. As shown in Fig. 6 a, the base alloy Mn30-T exhibits typical fully recrystallized features, with an average grain size of 5.2 μm, random crystallographic orientation, and well-defined grain boundaries. In Fig. 6 b, the Mn30-AlTi-T specimen demonstrates significant grain refinement, with the average grain size reduced to 1.52 μm while maintaining a uniform orientation distribution, indicating that Al/Ti microalloying alters the recrystallization behavior of the alloy. This grain refinement effect arises from three synergistic mechanisms: first, the solute drag effect induced by Al/Ti effectively suppresses grain boundary migration; second, the presence of nanoscale precipitates restricts grain growth through Zener pinning; and third, alloying elements significantly modify the ratio of nucleation rate to growth rate during recrystallization [20, 21]. Fig. 6 c shows that after aging at 600 °C for 4 h, the Mn30-AlTi-TA specimen exhibits a slight increase in average grain size to approximately 1.88 μm, while the orientation distribution remains largely similar to that of the purely annealed state, indicating that aging has a stabilizing effect on the recrystallized microstructure.

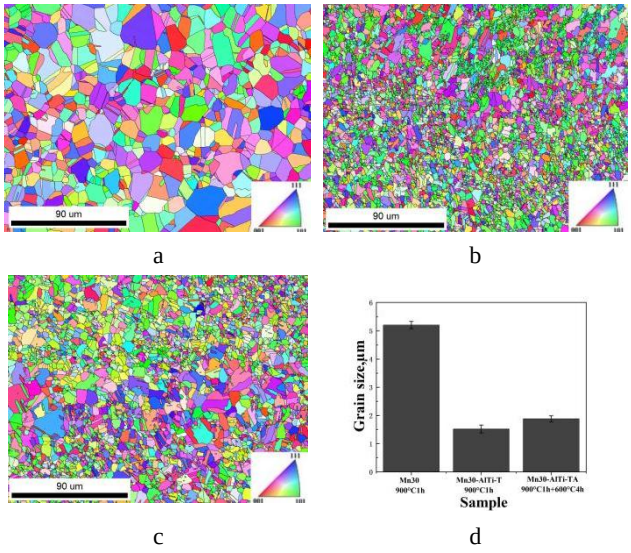

Fig. 6. EBSD IPF maps: a – Mn30-T; b – Mn30-AlTi-T; c – Mn30-AlTi-TA alloys; d – statistical diagram of grain size of the three alloys

Fig. 7 shows the phase maps of Mn30-T, Mn30-AlTi-T, and Mn30-AlTi-TA specimens. The base alloy Mn30-T maintains a single FCC phase structure, accounting for nearly 100 %, with no detectable secondary phase precipitation and a uniform phase distribution (Fig. 7 a). In the Mn30-AlTi-T specimen, a small amount of BCC phase (~0.7 %) precipitates, preferentially located at recrystallized grain boundaries, triple junctions, and deformation bands, corresponding to crystallographic defect regions (Fig. 7 b). After aging at 600 °C for 4 h, the Mn30-AlTi-TA specimen exhibits approximately 99.3 % FCC phase and 0.7 % BCC phase, with distribution characteristics similar to the solely annealed state (Fig. 7 c). Overall, Al/Ti microalloying effectively promotes the precipitation of the BCC phase.

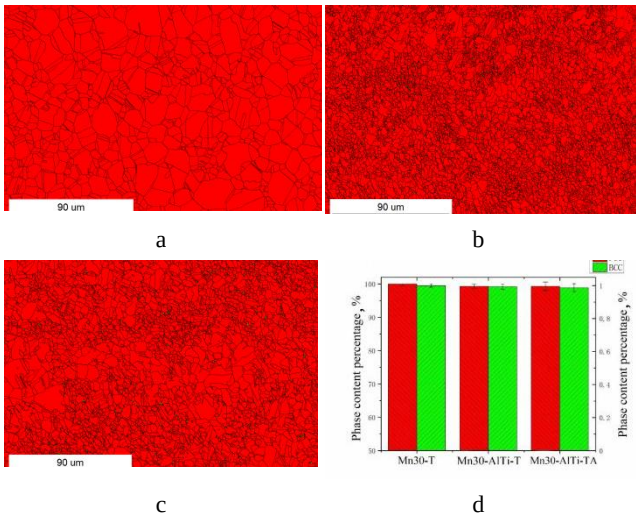

Fig. 7. EBSD phase maps: a – Mn30-T; b – Mn30-AlTi-T; c – Mn30-AlTi-TA alloys; d – statistical diagram of phase distribution of three alloys

Fig. 8 presents the Kernel Average Misorientation (KAM) maps of Mn30-T, Mn30-AlTi-T, and Mn30-AlTi-TA specimens, accompanied by KAM distribution curves for quantitative analysis.

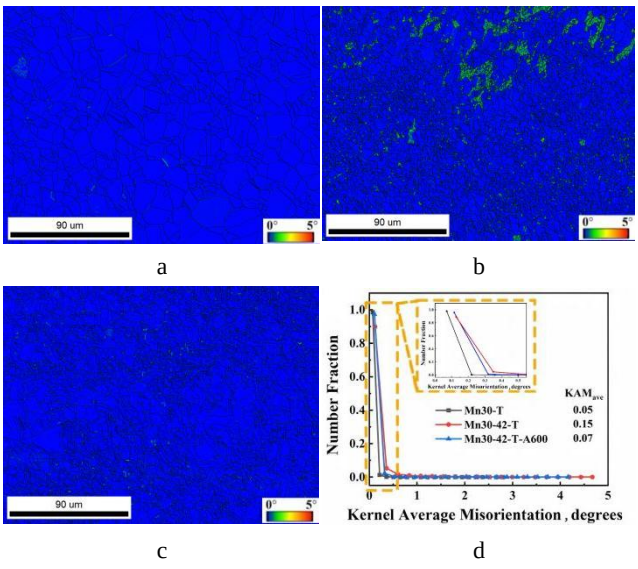

Fig. 8. KAM maps: e a – Mn30-T; b – Mn30-AlTi-T; c – Mn30-AlTi-TA alloys; d – KAM statistical diagram of three alloys

As shown in Fig. 8 a, the Mn30-T specimen exhibits a uniform KAM distribution with an average value of

approximately 0.05°, indicating that the fully recrystallized structure effectively reduces dislocation density. In Fig. 8 b, the Mn30-AlTi-T specimen shows a significantly increased KAM value, with a peak reaching 0.15°, and elevated dislocation density is observed in incompletely refined regions. This phenomenon is primarily attributed to local lattice distortions introduced by microalloying elements Al and Ti, residual dislocations from incomplete recrystallization, and heterogeneous distribution of deformation stored energy. After aging at 600 °C for 4 h, the Mn30-AlTi-TA specimen exhibits a decreased average KAM value of 0.07° with a more uniform distribution (Fig. 8 c), indicating that aging effectively relieves residual stresses, improves microstructural homogeneity, and promotes a reduction in dislocation density. Overall, the variations in KAM values not only confirm that Al/Ti microalloying increases the local strain energy of the alloy but also demonstrate that aging treatment effectively alleviates residual stresses.

Fig. 9 presents the recrystallization fraction maps of Mn30-T, Mn30-AlTi-T, and Mn30-AlTi-TA specimens, quantitatively characterized using statistical histograms. As shown in Fig. 9 a, the Mn30-T specimen exhibits an almost fully recrystallized structure, with a recrystallization fraction of 98.2 % and only 1.8 % recovery structure, indicating that the annealing parameters are sufficient to achieve complete recrystallization.

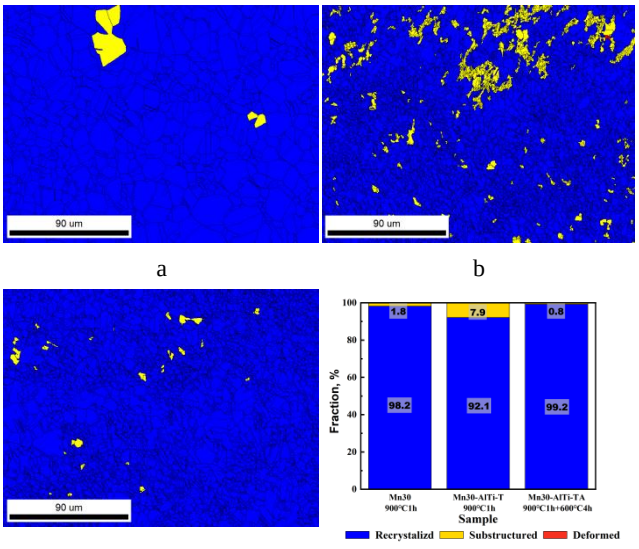

Fig. 9. GOS maps: a – Mn30-T; b – Mn30-AlTi-T; c – Mn30-AlTi-TA alloys; d – statistical diagram of recrystallization proportion of the three alloys

Fig. 9 b shows that the addition of Al/Ti alters the recrystallization behavior through microalloying, reducing the recrystallization fraction of Mn30-AlTi-T to 92.1 % while increasing the recovery fraction to 7.9 %. This change is primarily attributed to the solute drag effect induced by microalloying elements and the potential Zener pinning, which jointly hinder grain boundary migration and the growth of recrystallized grains. As shown in Fig. 9 c, after aging at 600 °C for 4 h, the Mn30-AlTi-TA specimen exhibits a further increase in recrystallization fraction to 99.2 %, with the recovery fraction decreasing to 0.8 %. This indicates that subsequent aging provides additional thermally activated energy, promoting the completion of recrystallization in residual deformed regions and thereby improving the uniformity of the microstructure.

3.3. HYDROGEN EMBRITTLEMENT RESISTANCE

Fig. 10 presents the stress–strain curves of Mn30-T, Mn30-AlTi-T, and Mn30-AlTi-TA specimens before and after hydrogen charging. The results show that, for the Mn30-T specimen in the uncharged state, the ultimate tensile strength (UTS), yield strength (YS), and elongation (EI) are 488 MPa, 158 MPa, and 36.1 %, respectively. After hydrogen charging, the UTS decreases by 4 % to 469 MPa, and the elongation drops by 14.4 % to 30.9 %, while the yield strength anomalously increases by 17 % to 185 MPa, resulting in a plasticity loss rate (δH) of 14.4 %.

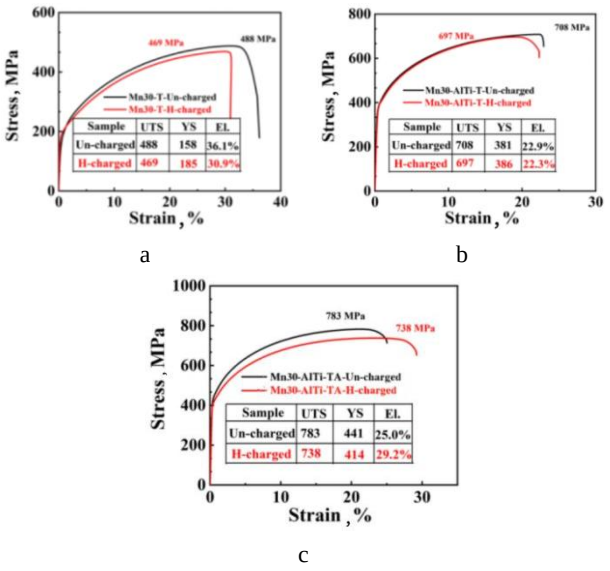

Fig. 10. Stress-strain curves: a – Mn30-T; b – Mn30-AlTi-T; c – Mn30-AlTi-TA alloys

For the Mn30-AlTi-T specimen in the uncharged state, UTS, YS, and EI are 708 MPa, 381 MPa, and 22.9 %, respectively. After hydrogen charging, the mechanical properties show minimal degradation: UTS decreases slightly by 1.6 % to 697 MPa, and EI marginally drops to 22.3 %, with δH of 2.6 %. Numerous studies [22 – 25] have indicated that Al/Ti microalloying can exert dual effects on the mechanical properties and hydrogen embrittlement resistance of medium-entropy alloys. The positive effect arises from nanoscale precipitates that hinder hydrogen diffusion and strengthen grain boundary cohesion, whereas the negative effect results from precipitate coarsening and hydrogen trap saturation. Compared with Mn30-T, the Mn30-AlTi-T specimen exhibits significantly enhanced performance because, due to the appropriate Al/Ti ratio and heat treatment, the positive mechanisms dominate, effectively improving both mechanical strength and hydrogen embrittlement resistance.

Notably, the Mn30-AlTi-TA specimen exhibits an excellent combination of strength and ductility even in the uncharged state, with UTS, YS, and EI of 783 MPa, 441 MPa, and 25.0 %, respectively. After hydrogen

charging, the UTS decreases slightly by 5.7 % to 738 MPa, while the elongation increases to 29.2 %, resulting in a negative plasticity loss rate (δH) of – 16.8 %. This indicates a "hydrogen-enhanced plasticity" effect in the specimen [26 – 28].

To investigate the influence of hydrogen on the fracture mechanisms of the $Cr_9Fe_{46}Ni_{15}Mn_{30}$ medium-entropy alloy, the fracture morphologies of the specimens before and after hydrogen charging were systematically characterized and analyzed. Fig. 11 shows the macroscopic fracture surfaces and the microstructural features of the edge and center regions for Mn30-T, Mn30-AlTi-T, and Mn30-AlTi-TA specimens.

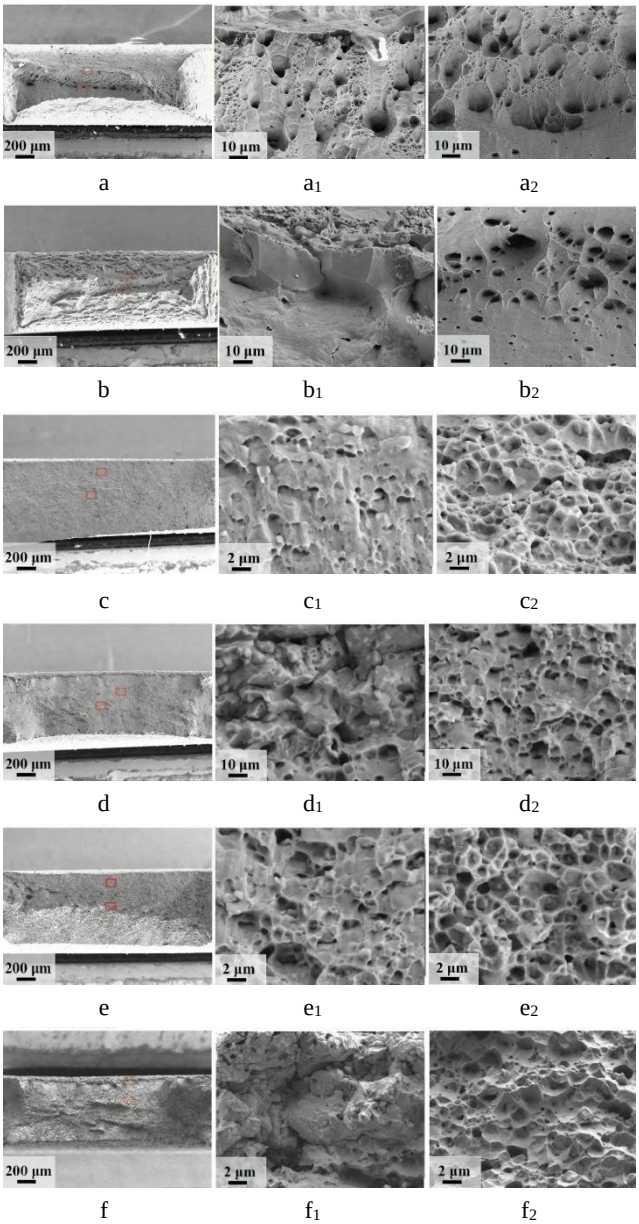

Fig. 11. Fracture surface morphologies: a – Mn30-T-Un-charged; b – Mn30-T-H-charged; c – Mn30-AlTi-T-Un-H-charged; d – Mn30-AlTi-T-H-charged; e – Mn30-AlTi-TA-A600-Un-charged; f – Mn30-AlTi-TA-H-charged

The uncharged samples of all three alloys exhibit typical ductile fracture characteristics, with uniformly distributed equiaxed dimples observed at both the edges and the centers (Fig. 11 a_2, a_3, c_2, c_3, e_2, e_3), indicating that fracture occurred through microvoid coalescence during plastic deformation. In contrast, the hydrogen-charged specimens display clear hydrogen-induced brittle fracture features, with a gradient distribution of fracture modes: the edge regions, identified as hydrogen-affected zones, exhibit intergranular fracture morphologies (Fig. 11 b_2, d_2, f_2), whereas the central regions retain ductile fracture characteristics (Fig. 11 b_3, d_3, f_3).

This dual-mode fracture behavior is attributed to the diffusion kinetics of hydrogen atoms from the surface to the interior during charging, resulting in a hydrogen concentration gradient from the edge to the center. Since the hydrogen diffusion depth is limited, the central regions have hydrogen concentrations below the critical embrittlement threshold, and their fracture mechanisms remain consistent with those of the uncharged specimens. Notably, the hydrogen-affected zone in the Mn30-AlTi-TA specimen is relatively small, suggesting that aging treatment may enhance hydrogen embrittlement resistance through grain boundary strengthening or hydrogen trap effects. These results indicate that hydrogen embrittlement susceptibility is closely related to hydrogen diffusion behavior and microstructural characteristics. The uniform dimple structure in uncharged samples confirms their excellent plastic deformation capability, whereas the intergranular fracture at the edges of hydrogen-charged samples highlights the dominant role of hydrogen-induced grain boundary weakening. The introduction of aging treatment likely optimizes grain boundary chemistry or introduces nanoscale precipitates, effectively suppressing hydrogen segregation at grain boundaries and thereby improving the alloy's resistance to hydrogen embrittlement.

3.4. CORROSION RESISTANCE

To further evaluate the corrosion resistance of the $Cr_9Fe_{46}Ni_{15}Mn_{30}$ medium-entropy alloys, Fig. 12 presents the electrochemical test results of Mn30-T, Mn30-AlTi-T, and Mn30-AlTi-TA specimens in 3.5 % NaCl solution, including potentiodynamic polarization curves and electrochemical impedance spectroscopy (EIS). The potentiodynamic polarization curves are shown in Fig. 12 a. The corrosion potentials (E_{corr}) of Mn30-T, Mn30-AlTi-T, and Mn30-AlTi-TA are –0.619 V, –0.308 V, and –0.279 V, respectively, while the corrosion current densities (Icorr) are 9.86×10^{-7} A·cm^{-2}, 6.47×10^{-7} A·cm^{-2}, and 6.39×10^{-7} A·cm^{-2}. These results indicate that the Mn30-AlTi-TA specimen exhibits the highest E_{corr} and the lowest I_{corr}. Numerous studies [29] have demonstrated that lower corrosion current density and more positive corrosion potential correspond to better corrosion resistance. Therefore, the Mn30-AlTi-TA specimen shows superior corrosion performance. It is noteworthy that the anodic branch exhibits significant passivation behavior over a potential range of approximately 600 mV above E_{corr}, indicating the formation of a protective oxide film on the alloy surface. However, transient current fluctuations observed within the passive region (indicated by arrows in Fig. 12 a) reveal the nucleation and repassivation processes of metastable pitting [30], which are typically associated with localized breakdown of the passive film and Cl^- attack.

The AC impedance spectra were analyzed using the equivalent circuit model shown in Fig. 12 b. In this model: R_s represents the solution resistance, R_{ct} denotes the charge transfer resistance, R_f indicates the resistance of the passive film, CPE_1 corresponds to the electrochemical double-layer capacitance, and CPE_2 represents the passive film capacitance.

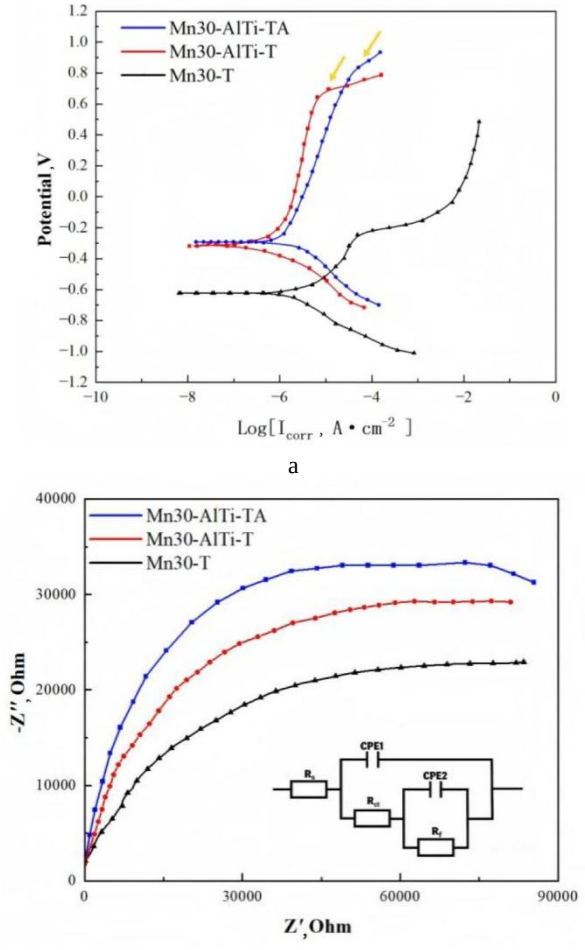

Fig. 12. a – potentiodynamic polarization curve; b – electrochemical AC impedance spectra and equivalent circuit model of $Cr_9Fe_{46}Ni_{15}Mn_{30}$ medium-entropy alloy

To account for the uneven surface morphology and energy dissipation of the electrode, a constant phase element (CPE) was introduced to simulate the capacitive behavior of the material more accurately. The impedance of the constant phase element (Q) is defined by the following formula:

$$Z_Q = \frac{1}{Y_0}(j\omega)^{-n} \quad (1)$$

where j is the imaginary unit ($j^2 = -1$); ω is the angular frequency ($\omega = 2\pi f$); Y_0 is the CPE constant;, n ($-1<n<1$) is the phase angle exponent, which describes the deviation from ideal capacitive behavior.

The Nyquist plots exhibit a depressed capacitive semicircle in the high-frequency region and an approximately linear feature in the low-frequency region. The semicircular response is attributed to charge-transfer-controlled electrochemical reactions, with the diameter of the semicircle corresponding to the charge transfer resistance. A larger high-frequency semicircle indicates a higher Rct value and, consequently, improved corrosion resistance. Accordingly, the Mn30-AlTi-T specimen exhibits the best corrosion performance among the investigated alloys. Furthermore, based on Zhang et al. [31], who observed a passive film–precipitate competition mechanism induced by Al addition in CoCrFeNi high-entropy alloys, it can be inferred that in the $Cr_9Fe_{46}Ni_{15}Mn_{30}$ medium-entropy alloy, Al enhances the stability of Cr_2O_3 within the passive film and increases the film thickness, thereby increasing Rct and slowing the dissolution rate of Fe^{2+}/Cr^{3+}. Additionally, aging treatment reduces dislocation density and improves microstructural uniformity (as shown in Fig. 5, Fig. 8, and Fig. 9), which further contributes to the enhancement of corrosion resistance.

4. CONCLUSIONS

1. Al/Ti microalloying refines the grain size of the $Cr_9Fe_{46}Ni_{15}Mn_{30}$ medium-entropy alloy from 5.2 μm to 1.52 μm, induces the formation of 50 – 500 nm Al/Ti-enriched nanoscale precipitates and ~0.7 % BCC phase, and increases the resistance to recrystallization, reducing the recrystallization fraction from 98.2 % to 92.1 % and increasing the KAM value from 0.05° to 0.15°. Subsequent aging treatment further promotes microstructural homogenization, raising the recrystallization fraction of Mn30-AlTi-TA to 99.2 %, lowering the KAM value to 0.07°, and optimizing precipitate distribution. The alloy maintains a single FCC structure throughout, and the combined effects of Al/Ti addition and aging treatment – through grain refinement, precipitate modulation, and stress relief – significantly enhance the overall properties.
2. Al/Ti microalloying effectively reduces hydrogen-induced plasticity loss in the $Cr_9Fe_{46}Ni_{15}Mn_{30}$ medium-entropy alloy by forming nanoscale precipitates that hinder hydrogen diffusion and strengthen grain boundary cohesion, lowering the δH value to 2.6 %. Subsequent aging treatment further optimizes the precipitate distribution and grain boundary structure, resulting in the Mn30-AlTi-TA specimen achieving a UTS of 738 MPa and an elongation of 29.2 % after hydrogen charging, with a δH of –16.8 %, exhibiting a pronounced "hydrogen-enhanced plasticity" effect. Fracture analysis indicates that hydrogen-induced embrittlement primarily manifests as intergranular fracture at the edges, whereas Al/Ti addition combined with aging effectively suppresses hydrogen segregation, reduces the hydrogen-affected zone, and significantly improves the alloy's resistance to hydrogen embrittlement.
3. Al/Ti microalloying significantly enhances the corrosion resistance of the $Cr_9Fe_{46}Ni_{15}Mn_{30}$ medium-entropy alloy, as evidenced by a positively shifted corrosion potential and a reduced corrosion current density. Subsequent aging treatment further improves the electrochemical performance, yielding the highest corrosion potential (–0.279 V) and the lowest corrosion current density (6.39×10^{-7} A·cm^{-2}) for the Mn30-AlTi-TA condition. Electrochemical impedance spectroscopy confirms that this specimen presents the largest capacitive arc radius, corresponding to the

highest charge transfer resistance. These enhancements are primarily attributed to the formation of a more stable and protective passive film induced by Al/Ti addition, together with a homogenized microstructure and reduced defect density resulting from aging treatment.

Acknowledgments

The authors gratefully acknowledge the support from the Open Fund of the Jiangsu Provincial Engineering Research Center for Autonomous Driving Technology (Grant No. ZK25-06-11). Yuanji Shi is indebted to the Financial Support from the QingLan Project of Jiangsu Province, China.

REFERENCES

1. **Dwivedi, S.K., Vishwakarma, M.** Hydrogen Embrittlement in Different Materials: A Review I*nternational Journal of Hydrogen Energy* 43 (46) 2018: pp. 21603 – 21616. https://doi.org/10.1016/j.ijhydene.2018.09.201
2. **Li, Y.Y., Wang, Q., Zhang, H.W., Zhu, H.Y., Wang, M.L., Wang, H.W.** Role of Solute Atoms and Vacancy in Hydrogen Embrittlement Mechanism of Aluminum: A First-principles Study *International Journal of Hydrogen Energy* 48 (11) 2023: pp. 4516 – 4528. https://doi.org/10.1016/j.ijhydene.2022.10.257
3. **Guo, Z.H., Liu, M., Ma, Y., Yu, H., Jing, S.R.** Hydrogen Embrittlement and Corrosion Resistance of NiCoCr-based Equimolar Face-centered Cubic Medium-/High-Entropy Alloys *Corrosion Science* 245 2025: pp. 112700. https://doi.org/10.1016/j.corsci.2025.112700
4. **Ma, Y., Yang, M.X., Yuan, F.P., Wu, X.L.** A Review on Heterogeneous Nanostructures: a Strategy for Superior Mechanical Properties in Metals *Metals* 9 (5) 2019: pp. 598. https://doi.org/10.3390/met9050598
5. **He, Q.F., Yang, Y.** Lattice Distortion in High-Entropy Alloys *Acta Metallurgica Sinica* 57 (04) 2021: pp. 385 – 392. https://doi.org/10.3389/fmats.2018.00042
6. **Kumar, A., Swarnakar, A.K., Basu, A., Chopkar, M.** Effects of Processing Route on Phase Evolution and Mechanical Properties of CoCrCuFeNiSix High Entropy Alloys *Journal of Alloys and Compounds* 748 2018: pp. 889 – 897. https://doi.org/10.1016/j.jallcom.2018.03.242
7. **He, J.Y., Wang, H., Huang, H.L., Xu, X.D., Chen, M.W., Wu, Y., Liu, X.J., Nieh, T.G., An, K., Lu, Z.P.** A Precipitation-hardened High-Entropy Alloy With Outstanding Tensile Properties *Acta Materialia* 102 2016: pp. 187 – 196. https://doi.org/10.1016/j.actamat.2015.08.076
8. **Qin, G., Chen, R.R., Liaw, P.K., Gao, Y.F., Li, X.Q., Zheng, H.T., Wang, L., Su, Y.Q., Guo, J.J., Fu, H.Z.** A Novel Face-Centered-Cubic High-Entropy Alloy Strengthened by Nanoscale Precipitates *Scripta Materialia* 172 2019: pp. 51 – 55. https://doi.org/10.1016/j.scriptamat.2019.07.008
9. **Takeuchi, A., Inoue, A.** Calculations of Mixing Enthalpy and Mismatch Entropy for Ternary Amorphous Alloys *Materials Transactions* 41 (11) 2000: pp. 1372 – 1378. https://doi.org/10.2320/matertrans1989.41.1372
10. **Bei, H.W., Wang, P.J., Ai, T.T.** Effect of Aging Treatment on L12 Precipitated Phase and Mechanical Properties of（FeNiCoCr）90 Al5 Ti5 High Entropy Alloy *Journal of Materials Engineering and Performance* 52 (04) 2024: pp. 146 – 154. https://doi.org/10.11868/j.issn.1001-4381.2023.000493
11. **Hong, L., Sohn, S.S., Lu, W.J., Li, L.L., Li, X.G., Soundararajan, C.K., Krieger, W., Liet, Z.M., Raabe, D.** A Strong and Ductile Medium-entropy Alloy Resists Hydrogen Embrittlement and Corrosion *Nature Communications* 11 (1) 2020: pp. 3081. https://doi.org/10.1038/s41467-020-16791-8
12. Li, Q., Mo, J.W., Ma, S.H., Duan, F.H., Zhao, Y.L., Liu, S.F., Liu, W.H., Zhao, S.J., Liu, C.T., Liaw, P.K., Yang, T. Defeating Hydrogen-induced Grain-boundary Embrittlement Via Triggering Unusual Interfacial Segregation in FeCrCoNi-Type High-entropy Alloys *Acta Materialia* 241 2022: pp. 118410. https://doi.org/10.1016/j.actamat.2022.118410
13. **Chen, H., Ma, Y.A., Li, C., Zhao, Q.Y., Huang, Y.H., Luo, H., Ma, H.C., Li, X.G.** A Nano-sized NbC Precipitation Strengthened FeCoCrNi High Entropy Alloy with Superior Hydrogen Embrittlement Resistance *Corrosion Science* 208 2022: pp. 110636. https://doi.org/10.1016/j.corsci.2022.110636
14. **Kwon, Y.J., Won, J.W., Park, S.H., Lee, J.H., Lim, K.R., Na, Y.S., Lee, C.S.** Ultrahigh-strength CoCrFeMnNi High-Entropy Alloy Wire Rod with Excellent Resistance to Hydrogen Embrittlement *Materials Science and Engineering* 732 2018: pp. 105 – 111. https://doi.org/10.1016/j.msea.2018.06.086
15. **Li, X.F., Feng, Z., Song, X.L., Wang, Y.F., Zhang, Y.** Effect of Hydrogen Charging Time on Hydrogen Embrittlement of CoCrFeMnNi High-entropy Alloy *Corrosion Science* 198 2022: pp. 110073. https://doi.org/10.1016/j.corsci.2021.110073
16. **Cheng, H.X., Luo, H., Pan, Z.M., Wang, X.F., Zhao, Q.Z., Li, X.G.** Hydrogen Embrittlement of a Precipitation-strengthened High-Entropy Alloy *Corrosion Science* 227 2024: pp. 111708. https://doi.org/10.1016/j.corsci.2023.111708
17. **Ding, N., Jin, S.J., Peng, L.M., Lei, M.K., Lin, L.** Ultrasonic Characterization of Recrystallized Microstructure Evolution for Al0.26CoCrFeNiMn High-Entropy Alloys *Journal of Materials Engineering* 47 (12) 2019: pp. 71 – 77. https://doi.org/10.11868/j.issn.1001-4381.2018.000557
18. **Rao, J.C., Diao, H.Y., Ocelík, V., Vainchtein, D., Zhang, C., Kuo, C., Tang, Z. Guo, W. Poplawsky, J.D., Zhou, Y., Liaw, P.K., De Hosson, J.T.M.** Secondary phases in AlxCoCrFeNi high-entropy alloys: An in-situ TEM heating study and thermodynamic appraisal *Acta Materialia* 131 2017: pp. 206 – 220. https://doi.org/10.1016/j.actamat.2017.03.066
19. **Zhao, Y.J., Grosswendt, F., Rajkowski, M., Gemagami, P., Poulain, R., Perrière, L., Couzinié, J.P., Weber, S., Laplanche, G., Li, T.** Formation of an Ordered Phase in Hcp Precipitates During Aging of Bcc HfNbTaTiZr High-entropy Alloy *Scripta Materialia* 262 2025: pp. 116634. https://doi.org/10.1016/j.scriptamat.2025.116634
20. **Wang, Y.H., Yuan, Y., Yu, J.B., Wu, H.H., Wu, Y., Jiang, S.H., Liu, X.J., Wang, H., Lv, Z.P.** Design for Thermal Stability of Nanocrystalline Alloys Based on High-

Entropy Effects Acta Metallurgica Sinica 57 (04) 2021: pp. 403 – 412. https://doi.org/10.11900/0412.1961.2020.00494

21. **Geng, Z.W., Li, X.L., Bai, C.Y., Luo, J.R., Song, M., Chen, C., Zhou, K.C.** Progress in Study of FeMnCoCr Matestable High-Entropy Alloy Toughening Pathways and Service Performance Under Hydrogen Environment at Cryogenic Temperature *The Chinese Journal of Nonferrous Metals* 34 (2) 2024: pp. 422 – 442. https://doi.org/10.11817/j.ysxb.1004.0609
22. **Seita, M., Hanson, J.P., Gradečak, S., Demkowicz, M.J.** The Dual Role of Coherent Twin Boundaries in Hydrogen Embrittlement *Nature Communications* 6 (1) 2015: pp. 6164. https://doi.org/10.1038/ncomms7164
23. **Bai, Y., Momotani, Y., Chen, M.C. Shibata, A., Tsuji, N.** Effect of Grain Refinement on Hydrogen Embrittlement Behaviors of High Mn TWIP Steel *Materials Science and Engineering A* 651 2016: pp. 935 – 944. http://dx.doi.org/10.1016/j.msea.2015.11.017
24. **Bai, Y., Tian, Y., Gao, S. Shibata, A., Tsuji, N.** Hydrogen Embrittlement Behaviors of Ultrafine-Grained 22Mn-0.6C Austenitic Twinning Induced Plasticity Steel *Journal of Materials Research* 32 2017: pp. 4592 – 4604. http://dx.doi.org/10.1557/jmr.2017.351
25. **Zan, N., Ding, H., Guo, X.F., Tang, Z,Y., Bleck, .** Effects of Grain Size on Hydrogen Embrittlement in a Fe-22Mn-0.6C TWIP Steel *International Journal of Hydrogen Energy* 40 2015: pp. 10687 – 10696. https://doi.org/10.1016/j.ijhydene.2015.06.112
26. **Gavriljuk, V.G., Shyvaniuk, V.M., Teus, S.M**. Hydrogen in Metallic Alloys─ Embrittlement and Enhanced Plasticity: a Review *Corrosion Reviews* 42 (3) 2024: pp. 267 – 301. https://doi.org/10.1515/corrrev-2022-0060
27. **Luo, H., Li, Z., Raabe, D.** Hydrogen Enhances Strength and Ductility of An Equiatomic High-Entropy Alloy *Scientific Reports* 7 (1) 2017: pp. 9892. https://doi.org/10.1038/s41598-017-10774-4
28. **Zhang, Q.R., Sun, Q.Q.** Hydrogen Enhanced Localized Plasticity: A Critical Review *Journal of Chinese Society for Corrosion and Protection* 45 (2) 2025: pp. 271 – 282. https://doi.org/10.11902/1005.4537.2024.184
29. **Shi, Y., Dai, Y., Gao, G.** Study of The Corrosion Process of a PEO-Treated Aluminum Alloy in Different Concentrations of NaCl *Materials and Technology* 56 (4) 2022: pp. 407 – 414. https://doi.org/10.17222/mit.2022.452
30. **Tang, Y.M., Zuo, Y., Wang, J.N., Zhao, X.H., Niu, B., Lin, B.** The Metastable Pitting Potential and Its Relation to The Pitting Potential for Four Materials in Chloride Solutions *Corrosion Science* 80 2014: pp. 111 – 119. https://doi.org/10.1016/j.corsci.2013.11.015
31. **Zhang, C.L., Huang, L.F., Li, S.X., Li, K., Lu, S.Y., Li, J.F.** Improved Corrosion Resistance of Laser Melting Deposited CoCrFeNi-series High-Entropy Alloys by Al Addition *Corrosion Science* 225 2023: pp. 111599. https://doi.org/10.1016/j.corsci.2023.111599